

# Flame Spray Deposition of Titanium Alloy-Bioactive Glass Composite Coatings

G.M. Nelson, J.A. Nychka, and A.G. McDonald

(Submitted February 8, 2011; in revised form April 30, 2011)

**Powders of titanium alloy (Ti-6Al-4V) and bioactive glass (45S5) were deposited by flame spraying to fabricate composite porous coatings for potential use in bone fixation implants. Bioactive glass and titanium alloy powder were blended and deposited in various weight fractions under two sets of spray conditions, which produced different levels of porosity. Coatings were characterized with cross-sectional optical microscopy, x-ray diffraction (XRD), scanning electron microscopy (SEM), and Fourier transform infrared spectroscopy (FTIR). Immersion testing in simulated body fluid (SBF) was conducted for 0, 1, 7, and 14 days. Hydroxyapatite (HA) was found on the bioactive glass-alloy composite coatings after 7 days of immersion; no HA was observed after 14 days on the pure titanium alloy control coating. The HA formation on the alloy-bioactive glass composite coating suggests that the addition of bioactive glass to the blend may greatly increase the bioactivity of the coating through enhanced surface mineralization.**

**Keywords** bioactive glass, composite coating, flame spraying, mineralization

## 1. Introduction

Biomedical implants are typically made of bio-inert or bioactive materials. The most common biomedical implant material is titanium and its alloys, specifically Ti-6Al-4V (Ref 1). When a titanium implant is placed in the human body, there is often fibrous encapsulation of the implant, which may lead to loosening and pre-mature failure (Ref 2-4). Titanium has only been shown to promote cell growth after specialized surface preparation. Other studies have used methods such as sodium hydroxide (NaOH) surface treatment at an elevated pressure or micro patterning, in order to change surface properties and structure (Ref 5, 6).

Biomedical materials also include bioactive materials. Two common bioactive ceramics are 45S5 bioactive glass and hydroxyapatite (HA). Bioactive materials promote a cellular response, resulting in attachment of cells to the surface of the implant (Ref 2-4, 7). Bioactive glass and HA, which are ceramics, have the disadvantage of being brittle and unsuitable for load bearing applications. A study by Hench (Ref 2) found that it was not the presence of HA that was responsible for the cellular response,

but rather the release rates of ions from the dissolution of the bioactive glass. The dissolution of the bioactive glass induces the crystallization of HA and cellular growth. HA deposited alone may not cause the same process to occur (Ref 2). Bioactivity can be assessed in vitro through the use of simulated body fluid (SBF). This is an acceptable proxy because the first stages of the processes that result in cellular attachment can be simulated in the fluid (Ref 8).

Titanium implants typically require treatment to induce bioactivity of their surfaces (Ref 5, 6, 9). Surface treatments are typically expensive and labor-intensive. For example, Ou et al. (Ref 9) used an oxygen plasma oxidation technique to create an amorphous bioactive oxide surface layer. Thermal spraying—a manufacturing process that is used to fabricate thin coatings on a variety of solid surfaces—may be used to modify the surface to promote bioactivity. In this process, powder particles are introduced into a high-temperature flame or plasma, where they are melted, accelerated, and deposited on a surface to produce a thin layered coating. Other studies have prepared composites of bioactive materials and titanium and its oxides through air plasma spraying (APS) (Ref 1, 10, 11) and high-velocity oxy-fuel (HVOF) spraying (Ref 12, 13). These studies found evidence of surface bioactivity in vitro. However, APS and HVOF spraying are more expensive than flame spraying. Flame spraying is a process in which the combustion of acetylene ( $C_2H_2$ ) and oxygen ( $O_2$ ) produces a high-temperature flame to facilitate fabrication of the coatings for the purposes of surface modification.

A review of previous studies has shown that limited work has been conducted on the fabrication of a composite coating of bioactive glass and Ti-6Al-4V for biomedical implants. A study by Verne et al. (Ref 10) used a sintered composite of bioactive glass and titanium powder that was ground and deposited by APS. Flame spray deposition of a mechanical blend of powder eliminates the

**G.M. Nelson** and **J.A. Nychka**, Department of Chemical and Materials Engineering, University of Alberta, 7th Floor, Electrical & Computer Engineering Research Facility, Edmonton, AB T6G 2V4, Canada; and **A.G. McDonald**, Department of Mechanical Engineering, University of Alberta, 4-9 Mechanical Engineering Building, Edmonton, AB T6G 2G8, Canada. Contact e-mail: jnychka@ualberta.ca.

preparation and milling of a sintered composite. The additional cost of APS is also eliminated.

In this study, the effect of two sets of flame spray conditions and different powder blend compositions of Ti-6Al-4V and bioactive glass on the microstructure and phases of the final coating are assessed. One set of spray parameters and one composition were selected from a test matrix for further study. The thickness, porosity, and bioactive glass content of the selected coatings were examined. In addition, the bioactivity of both the composite coating and a pure Ti-6Al-4V alloy control was assessed in order to ascertain if the addition of bioactive glass resulted in a greater degree of bioactivity through surface mineralization. The porosity was examined to determine if osseointegration could be possible and to modify future spray conditions. Mechanical stability and quantification of bio-mineralization rate was beyond the scope of this study.

## 2. Experimental Method

### 2.1 Thermal Spraying

**2.1.1 Spray Conditions.** In this study, two sets of spray parameters were used for flame spray deposition. An oxy-acetylene flame spray torch (6PII ThermoSpray Gun, Sulzer Metco Inc., Westbury, NY) was operated under two sets of parameters, these parameters will be referred to as “low temperature” and “high temperature.” Table 1 includes the flow rate of O<sub>2</sub>, C<sub>2</sub>H<sub>2</sub>, and argon for each set of parameters. The flame spray torch was mounted on a robot (HP20, Motoman Inc., West Carrollton, OH) that was operated at a velocity of 400 mm/s for both sets of spray parameters. The powder feed rate varied between 60 and 90 FMR (flow meter reading) on a volumetric powder feeder (5MPE Powder Feeder, Sulzer Metco, Inc., Westbury, NY). The number of passes of the torch was varied between 5 and 10.

**2.1.2 Coatings Fabricated Under the High- and Low-Temperature Spray Conditions.** 45S5 bioactive glass (Mo-Sci Health Care, Rolla, MO) powder (derived from a melt casting route) was sieved to a size range of 106–212 μm (−212+106 μm) with a Ro-Tap powder sieve (RX-29-CAN, W.S. Tyler, Mentor, OH). Two blends of titanium alloy (Ti-6Al-4V) (5573-S, Raymor Industries, Boisbriand, QC, Canada) and 45S5 bioactive glass were prepared. The 45S5 bioactive glass powder and Ti-6Al-4V powder were placed in a 1 L Nalgene® polymeric bottle in the indicated amounts, see Table 2. The bottles were inverted and shaken end over end for 15 min. Additional mixing occurred in the volumetric powder feeder by using an air

vibrator. The titanium alloy powder had a size range of <45 μm (−45 μm). Titanium substrates, with a thickness of 1.6 mm (CP-Ti grade 2, McMaster-Carr, Chicago, IL) were cut into 25 × 12 mm coupons using a slow speed saw (TechCut 4, Allied High Tech Products, Inc., Rancho Dominguez, CA) and a metal-bonded diamond wafering blade (Allied High Tech Products, Inc., Rancho Dominguez, CA). The titanium substrates were grit-blasted (Trinco Dry Blast, Trinco Tool Co., Fraser, IL) with #24 grit alumina (686 μm Al<sub>2</sub>O<sub>3</sub>, Treibacher Schleifmittel North America, Inc., Niagara Falls, NY). The substrates were clamped to the substrate holder and cleaned with compressed air prior to deposition. The blends were deposited with the oxy-acetylene flame spray torch on to the prepared titanium substrates. Both blends, along with a pure bioactive glass and a pure titanium alloy powder sample, were deposited with both the high-temperature and low-temperature spray conditions.

The low-temperature spray conditions were used to fabricate Ti-6Al-4V alloy (control) and Ti-6Al-4V-bioactive glass composite coatings. The composite coating was fabricated from a powder composition similar to the 85/15 blend (Table 2). The bioactive glass powder was sieved to a size range of 45–90 μm (−90+45 μm) after it was ball-milled with cylindrical alumina media (20.6-mm diameter Al<sub>2</sub>O<sub>3</sub>, US Stoneware, East Palestine, OH) for 5 h. The coated titanium samples were stored in a desiccator cabinet (Secador, Fisher Scientific, Ottawa, ON, Canada) after deposition.

### 2.2 Coating Characterization

An SEM (Evo MA 15, Carl Zeiss Inc., Toronto, ON, Canada) was used to characterize the morphology of the Ti-6Al-4V and bioactive glass feed powders. The Ti-6Al-4V powder was characterized as received; the bioactive glass powder was characterized as received and as milled. The bioactive glass powder was coated with gold (SEM-prep II DC sputter coater, NanoTech, Prestwich, Manchester, UK). The powders were imaged in secondary electron (SE) mode with a LaB6 filament operating at a voltage of 10 kV.

The coated titanium substrates were mounted in cold-mount epoxy (EpoxySet, Allied High Tech Products Inc., Rancho Dominguez, CA) and cured overnight (approximately 10 h). The epoxy-mounted samples were ground (TwinPrep 3, Allied High Tech Products, Inc., Rancho Dominguez, CA) with silicon carbide grit paper (SiC Grit Paper, Allied High Tech Products, Inc., Rancho Dominguez, CA). The grit sizes used were in the sequence 240,

**Table 1** Flame spraying conditions

Condition	Oxygen flow rate, NLPM	Acetylene flow rate, NLPM	Argon flow rate, NLPM	Standoff distance, mm
High temperature	35	22	9.5	100
Low temperature	25	15	9.5	150

**Table 2** Powder blends

Blend	Mass of bioactive glass, g	Mass of Ti-6Al-4V, g
85 wt.% Ti-6Al-4V (78 vol.%)	80	533
15 wt.% 45S5 bioactive glass (22 vol.%)		
62 wt.% Ti-6Al-4V (50 vol.%)	232	380
38 wt.% 45S5 bioactive glass (50 vol.%)		

320, 400, 600, 800, and 1200. The samples were polished (Imperial Polishing Pads, Allied High Tech Products, Inc., Rancho Dominguez, CA) with a diamond suspension (Polycrystalline Diamond Suspension Water-based, High Tech Products, Inc., Rancho Dominguez, CA). The diamond sizes used were 3, 1, and 0.25  $\mu\text{m}$ . The samples prepared under the high-temperature and low-temperature conditions were viewed with an optical microscope (Epiphot 300, Nikon Corporation, Markham, ON, Canada). Micrographs ( $4288 \times 2848$  pixels) were taken with a digital camera (D300 Camera, Nikon Corporation, Markham, ON, Canada). The micrographs were taken in bright field (BF) mode, with an exposure time of 5 ms. A total of 40 micrographs were taken (five micrographs for each sample composition for each spray condition).

The alloy-bioactive glass samples, deposited under the low-temperature spray conditions with milled bioactive glass powder, were mounted using dyed epoxy (Oracet Blue, Met Tech, Calgary, AB, Canada) to provide better contrast between the bioactive glass particles and the pores in the coating. The polished samples were viewed with an optical microscope (Axio Imager M2m, Carl Zeiss, Inc., Toronto, ON, Canada). Micrographs ( $2776 \times 2080$  pixels) were taken with a high dynamic range pixel shifting digital camera (Axiocam HRc, Carl Zeiss Inc., Toronto, ON, Canada). BF images, with an exposure time of 9 ms, and ultraviolet fluorescent images (UV FL; excitation of 350 nm), with an exposure time of 60 ms, were taken. The UV FL images were used to identify pores filled with epoxy. The micrographs were analyzed using Image Pro software (Media Cybernetics, Bethesda, MD) using the Count and Measure feature to determine the porosity, bioactive glass content, and thickness of the coating. For this analysis, 12 images (6 per sample) were used for the control and 7 (3 and 4 for each sample) images were used for the alloy-glass composite.

The samples produced under both spray conditions were analyzed with x-ray diffraction (XRD) (RU-200B Line Focus X-ray System, Rigaku Rotating Anode XRD System, Rigaku, ON, Canada). The patterns were solved with the Jade 7 software (Jade 7, Materials Data, Inc., Livermore, CA). A continuous reflective XRD mode was used in which the  $2\theta$  angle was changed at a rate of  $3^\circ$  per minute. The XRD machine employed a Cu anode operated at 40 kV and 110 mA.

In addition, for the low-temperature samples produced from both milled bioactive glass powder and Ti-6Al-4V powder, an SEM with EDX (Silicon Drift Detector, Bruker, East Milton, ON, Canada), and a FTIR spectrometer (Nicolet Magna-IR Spectrometer 750, Thermo Scientific, Newington, NH) were employed. The SEM was used to image the features of the surface layer and to indicate changes in surface composition. The samples were carbon coated using a carbon evaporator (EM SD005, Leica, Richmond Hill, ON, Canada). Samples were imaged at  $100\times$ ,  $1000\times$ , and  $40,000\times$  magnification in both SE and backscattered electron (BSE) image modes at a tilt of  $30^\circ$ . EDX spectra were captured over a  $6.05 \text{ mm}^2$  area. A potassium bromide (KBr) pellet method was used to prepare the sample for the FTIR analysis.

The coating was planed from the substrate using a razor blade to obtain powder from the sample to be mixed with KBr powder (Xymotech Biosystems, Inc., Cote Saint-Luc, QC, Canada) and compressed into a spherical pellet. The pellets were run in absorbance transmittance mode with 32 scans and a resolution of  $4 \text{ cm}^{-1}$ . The scan range was between 400 and  $4000 \text{ cm}^{-1}$ .

### 2.3 Assessment of Bioactivity

SBF was prepared according to the formulation and method developed by Kokubo and Takadama (Ref 8). In preparation for immersion, the samples were rinsed with 5 mL of pure isopropyl alcohol ( $\text{C}_3\text{H}_8\text{OH}$ ), and then with 5 mL of de-ionized ultra-filtered water (DIUF). The samples were placed in 25 mL Petri dishes and the SBF was added. The Petri dishes were held at  $36.5 \pm 1.5^\circ\text{C}$  in a water bath (Isotemp 210, Fisher Scientific, Ottawa, ON, Canada). In this study, the coatings were exposed to the SBF solution for 1, 7, and 14 days. The sample surface area to SBF volume ratio was maintained at  $0.14 \text{ cm}^{-1}$  and the SBF solution was changed every 3 days, according to the procedures developed by Kokubo and Takadama (Ref 8). After the testing was completed, the samples were rinsed with 5 mL of DIUF and 5 mL of pure  $\text{C}_3\text{H}_8\text{OH}$ . The samples were allowed to dry in air overnight before being placed into a desiccator cabinet. Only the 15 wt.% alloy-bioactive glass composite and pure Ti-6Al-4V alloy samples that were prepared with the low-temperature spray conditions were immersed in SBF (further explanation to follow).

The samples were assessed for the presence of hydroxyl apatite (HA) ( $\text{Ca}_{10}(\text{PO}_4)_6(\text{OH})_2$ ) as an in vitro bioactivity indicator, using three techniques: scanning electron microscopy (SEM) with energy dispersive x-ray spectroscopy (EDX), Fourier transform infrared spectroscopy (FTIR), and XRD. For each technique, one sample was analyzed at each exposure time for each coating type.

## 3. Results and Discussion

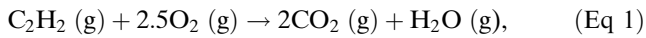
### 3.1 Flame Temperature Under High- and Low-Temperature Spray Conditions

The temperature of the flame in combustion flame spraying depends on the spray parameters of the torch. In particular, the flow rates of  $\text{C}_2\text{H}_2$  and  $\text{O}_2$  into the combustion process, as well as the volume of air entrained into the high-speed flame jet will have an impact on the flame temperature. The flame temperature will play a role on the degree of melting of the particles injected into the jet and on the final microstructure of the coating. While it is difficult to measure and estimate the true temperature of combustion flames, differences in the adiabatic flame temperature—the maximum possible temperature that can be achieved by the products of combustion with no heat loss—can be used to provide a qualitative understanding of the impact of high- and low-temperature spray conditions on the final alloy-bioactive glass composite

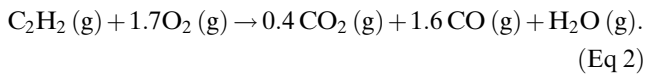


coating. The true flame temperature will be lower than the adiabatic flame temperature due to heat loss to the ambient, air entrainment, and the formation of nitrogen oxide (NO<sub>x</sub>) products.

In the complete, stoichiometric combustion of C<sub>2</sub>H<sub>2</sub> with theoretical O<sub>2</sub>, the balanced chemical reaction is



with carbon dioxide and water being formed as the only products. Under the low-temperature spray conditions, 15 NLPM of C<sub>2</sub>H<sub>2</sub> and 25 NLPM of O<sub>2</sub> were used. If the gases are assumed to be ideal, there were 1.7 mol of O<sub>2</sub> for every mole of C<sub>2</sub>H<sub>2</sub>. Under the high-temperature spray conditions, 22 NLPM of C<sub>2</sub>H<sub>2</sub> and 35 NLPM of O<sub>2</sub> were used, resulting in 1.6 mol of O<sub>2</sub> for every mole of C<sub>2</sub>H<sub>2</sub>. Based on reaction (1), 2.5 mol of O<sub>2</sub> are required to complete the reaction to form carbon dioxide and water vapor as products. For both the high- and low-temperature spray conditions, an O<sub>2</sub> deficiency exists, and carbon monoxide will be formed. For the low-temperature spray conditions, the balanced combustion reaction is



This incomplete combustion reaction will produce lower flame temperatures than that of reaction (1). It is also expected that due to the lower mole ratio of O<sub>2</sub> and C<sub>2</sub>H<sub>2</sub> under the high-temperature conditions, the flame temperature should be lowered even further. While not detected, there is potential that the lower mole ratio of O<sub>2</sub> and C<sub>2</sub>H<sub>2</sub> may produce small amounts of ultra-fine particles of carbon (soot) in the incomplete combustion of C<sub>2</sub>H<sub>2</sub>, which could contaminate the coatings.

The first law of thermodynamics can be applied to a constant, steady flow of gases and combustion in an open ambient to estimate the adiabatic flame temperature of the jet. Assuming no heat loss ( $Q_{\text{out}}=0$ ) and that the reactants are at 298 K, the law is given as

$$Q_{\text{out}} = 0 = \sum N_r \bar{h}_{f,r,298\text{K}}^\circ - \sum N_p (\bar{h}_{f,298\text{K}}^\circ + \bar{h} - \bar{h}_{298\text{K}}^\circ), \quad (\text{Eq 3})$$

where  $N$  is the number of moles,  $\bar{h}_{f,298\text{K}}^\circ$  is the standard enthalpy of formation at 298 K,  $\bar{h}_{298\text{K}}^\circ$  is the standard enthalpy measured at 298 K, and  $\bar{h}$  is the enthalpy at a temperature other than 298 K. Since the reactants were assumed to be at 298 K,  $(\bar{h} - \bar{h}_{298\text{K}}^\circ)_r = 0$ . The enthalpy,  $\bar{h}$  cannot be determined directly. However, since  $\bar{h} = \bar{h}(T)$ , it is possible to determine the adiabatic flame temperature of the combustion products and the flame through the use of thermodynamic tables and iteration. Enthalpy data for use in Eq 3 are presented in Table 3 (Ref 14). Substituting the enthalpy data into Eq 3 and using mole values from reaction (2) gives

$$830,326 \text{ kJ} = 0.4\bar{h}_{\text{CO}_2} + 1.6\bar{h}_{\text{CO}} + \bar{h}_{\text{H}_2\text{O}}. \quad (\text{Eq 4})$$

An initial estimation of the adiabatic flame temperature can be obtained by dividing the energy in Eq 4

**Table 3 Enthalpy data (Ref 14)**

Gas	$\bar{h}_{f,298\text{K}}^\circ$ , kJ/kmol	$\bar{h}_{298\text{K}}^\circ$ , kJ/kmol
C <sub>2</sub> H <sub>2</sub> (g)	+226,730	...
O <sub>2</sub>	0	8682
CO <sub>2</sub>	-393,520	9364
CO	-110,530	8669
H <sub>2</sub> O (g)	-241,820	9904

(830,326 kJ) by the total number of moles (3 kmol) of product. The enthalpy that will be used as an initial guess of the adiabatic flame temperature is 276,775 kJ/kmol. Three different temperatures will be expected due to the three different gas species that are present in the combustion product. However, given that larger quantities of carbon monoxide and water are present in the flame, it is expected that their temperatures will dominate the overall flame temperature. A weighted average temperature was calculated for the three gas temperatures at 276,775 kJ/kmol, and it was used to determine the gas enthalpies. The gas enthalpies were used to verify if both sides of Eq 4 were balanced. After further iterations to balance Eq 4, it was found that the adiabatic flame temperature for the low-temperature spray conditions was approximately 6040 °C. A similar procedure was employed for the high-temperature spray conditions to give an adiabatic flame temperature of 5830 °C.

The difference in the maximum temperature of the flame under the low- and high-temperature spray conditions (210 °C) is small compared to the maximum temperatures. Therefore, any difference observed in the flame temperatures will be due to other factors. In this study, the stand-off distance under the low-temperature spray conditions (150 mm) was larger than that under the high-temperature spray conditions (100 mm). Larger stand-off distances will result in larger volumes of cold air entering the flame, as well as larger heat loss values due to greater flame surface area exposed to colder air. As cold air becomes entrained in the flame jet and heat is lost from the flame, the true flame temperatures will decrease. Therefore, it is expected that under the high-temperature spray conditions, the flame temperature should be higher due to lower heat loss and less entrainment of cold ambient air. It is also expected that the actual flame temperatures will be lower than the adiabatic flame temperatures due to heat loss from the flame and the entrainment of cold air into the flame jet.

### 3.2 Coating Characterization

**3.2.1 Implications of Flame Temperature Under High- and Low-Temperature Spray Conditions.** The morphology of the Ti-6Al-4V and bioactive glass powder was characterized by SEM. The bioactive glass micrographs were adjusted to the same scale as the alloy powder micrographs through image processing. The Ti-6Al-4V powder was spherical in shape (see Fig. 1, left images). The bioactive glass powder as received was jagged and angular, after milling the powder was similar in shape (see Fig. 1, right images).

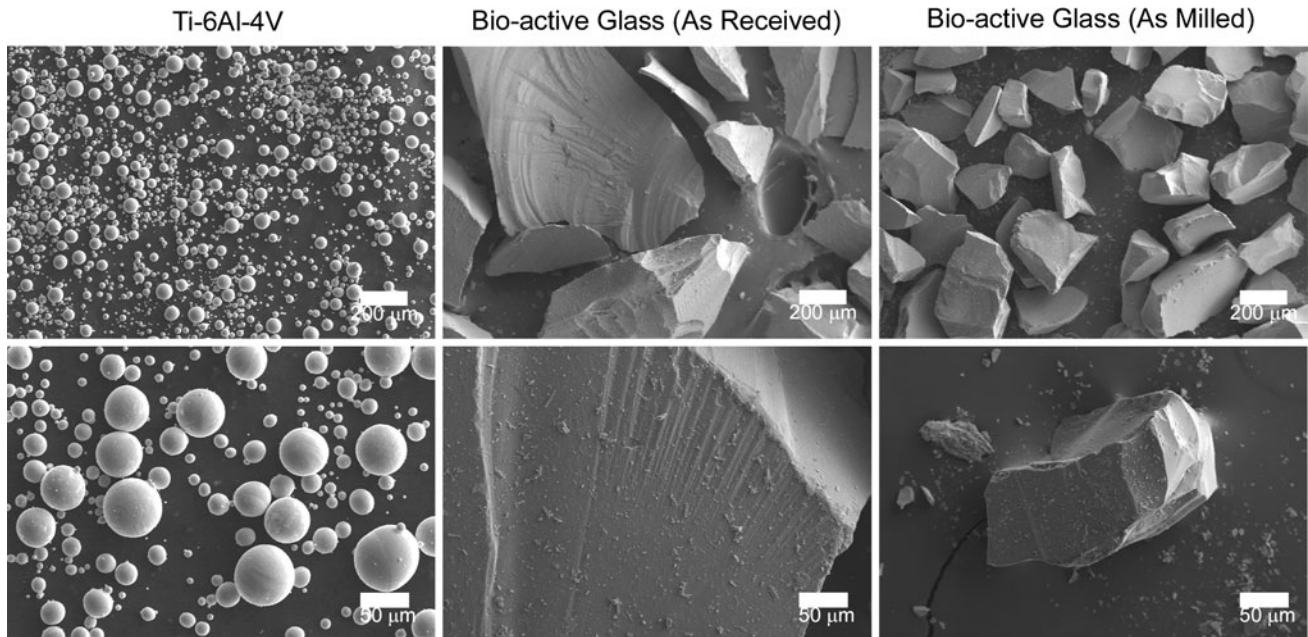
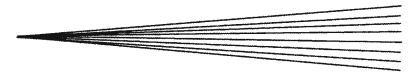


**Fig. 1** SEM micrographs of powder morphology. Left: Ti-6Al-4V, center: bioactive glass (as received), and right: bioactive glass (as milled)

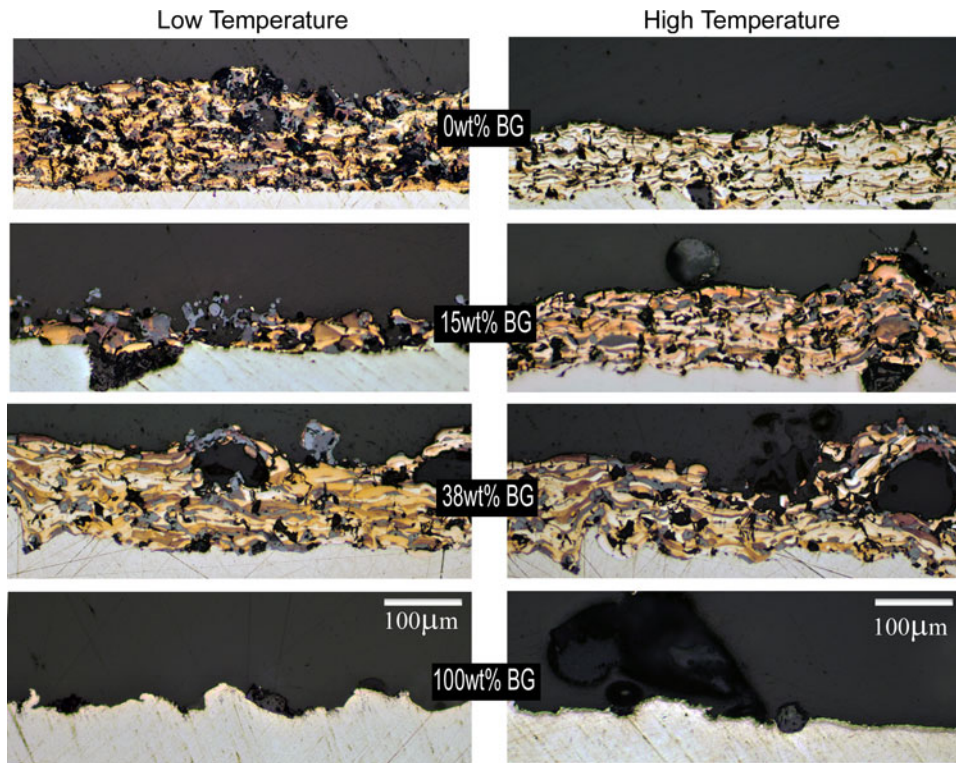


**Fig. 2** Optical cross-sectional micrographs of high- and low-temperature sample. Left: low temperature and right: high temperature

Coatings of bioactive glass blended with Ti-6Al-4V and the control coatings (pure bioactive glass and pure Ti-6Al-4V) were deposited by flame spraying onto titanium substrates. Both high-temperature and low-temperature spray conditions were used. The coatings were examined with

optical microscopy, and images are presented in Fig. 2. The pure bioactive glass did not adhere well to the substrate for either set of spray conditions, leaving only a scattering of glass particles on an otherwise bare substrate. When 38 wt.% bioactive glass was mixed with Ti-6Al-4V,

the composite coating exhibited a rough and porous microstructure for both spray conditions. The coating was continuous (see Fig. 2). However, the distribution of bioactive glass through the coating was not homogenous. In the composite coatings containing 15 wt.% bioactive glass, the glass distribution throughout the sample was more homogenous than that of the composite coatings with 38 wt.% bioactive glass. However, in the high-temperature spray condition; there was no visual evidence of pore connectivity within the cross section. The pure Ti-6Al-4V coating deposited under the high-temperature spray conditions exhibited a more compact and less porous coating

than that deposited under the low-temperature spray conditions.

The samples were also analyzed with XRD and the profiles are presented in Fig. 3(a). The background on the profiles have been stripped and filtered. A representative raw profile has also been included in Fig. 3(b). Peak assignments were determined according to the guidelines provided in the Jade 7 XRD database. The pure bioactive glass coatings exhibited peaks for combeite ( $\text{Na}_2\text{Ca}_2\text{Si}_3\text{O}_3$ ), titanium sub-oxide ( $\text{TiO}_{0.89}$ ), titanium, and anatase phase of titanium dioxide ( $\text{TiO}_2$ ).  $\text{TiO}_2$  was present due to oxidation of the titanium substrate.  $\text{Na}_2\text{Ca}_2\text{Si}_3\text{O}_3$  is the

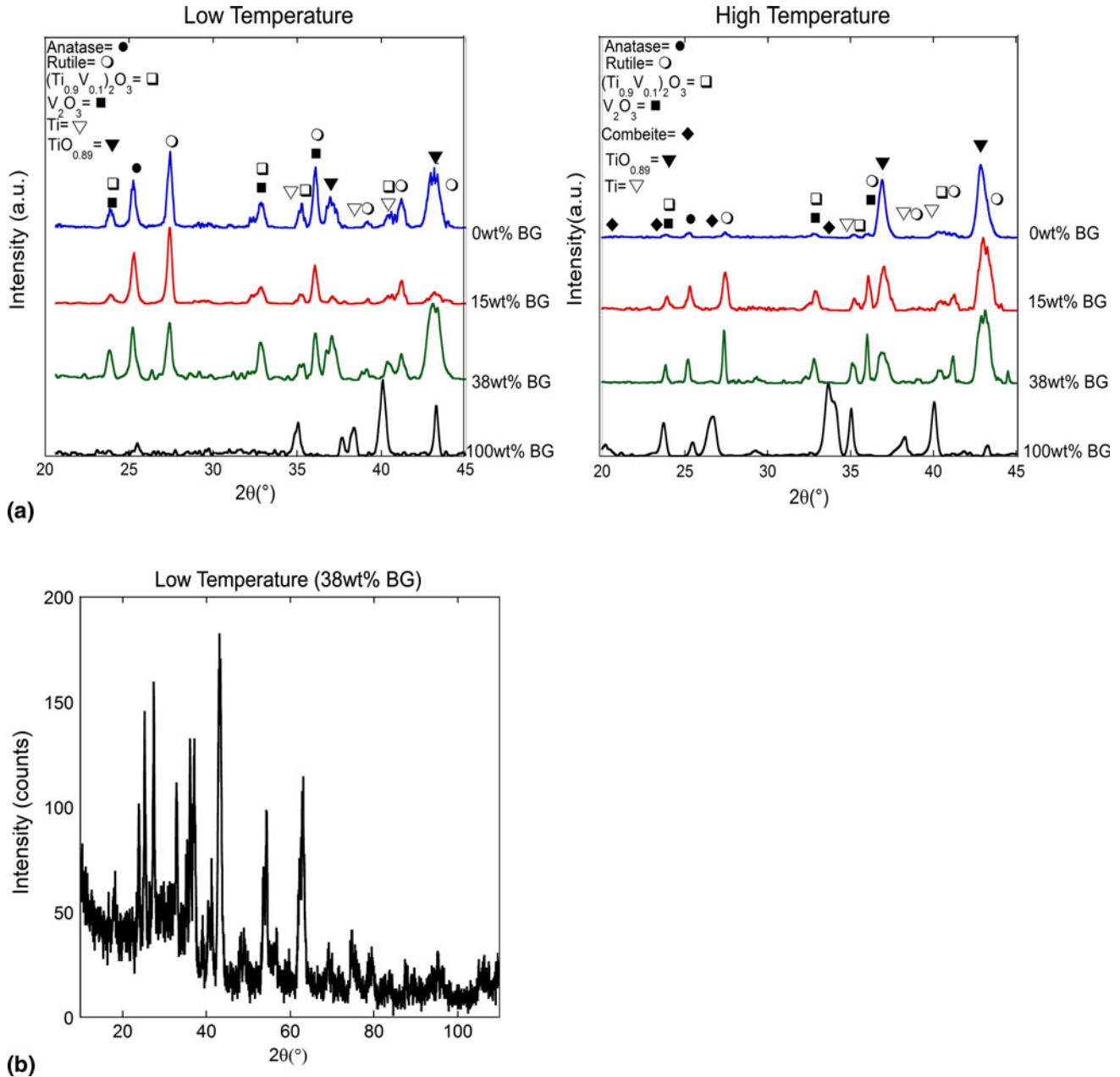


**Fig. 3** (a) XRD patterns of high- and low-temperature sample. Left: low temperature, right: high temperature and (b) representative raw XRD pattern



crystalline phase of bioactive glass. The  $\text{Na}_2\text{Ca}_2\text{Si}_3\text{O}_3$  peaks were present only in the coatings deposited under the high-temperature spray conditions. No  $\text{Na}_2\text{Ca}_2\text{Si}_3\text{O}_3$  peaks were present in the bioactive glass coatings deposited under the low-temperature spray conditions (see Fig. 3a). The absence of  $\text{Na}_2\text{Ca}_2\text{Si}_3\text{O}_3$  peaks indicates that the bioactive glass remained amorphous during the spray process. The presence of  $\text{Na}_2\text{Ca}_2\text{Si}_3\text{O}_3$  indicated that the bioactive glass was heated above its recrystallization point (650–700 °C) during deposition (Ref 15, 16). The cross-sectional micrographs (see Fig. 2) indicate that the bioactive glass is spherical in shape. The spherical shape differs from the usual angular and jagged shapes of the initial glass powder (see Fig. 1, right images). Therefore, the bioactive glass, in both sets of spray conditions, was heated above the softening temperature of the bioactive glass (which is higher than the recrystallization temperature). The heated bioactive glass changed from a jagged shape to a spherical shape to minimize surface energy. A previous study by Nychka et al. (Ref 17) indicated that the dissolution rate of bioactive glass in a crystalline form is slower than its amorphous form in an in vitro environment. As such, the crystallization of the bioactive glass during the high-temperature deposition would likely lead to a lesser bioactive response.

The pure Ti-6Al-4V coating, composite coating with 15 wt.% bioactive glass, and the composite coating with 38 wt.% bioactive glass all exhibited similar XRD profiles. The samples primarily exhibited peaks for titanium,  $\text{TiO}_{0.89}$ , anatase and rutile phases of  $\text{TiO}_2$ , vanadium oxide ( $\text{V}_2\text{O}_3$ ), and titanium vanadium oxide ( $\text{Ti}_{0.9}\text{V}_{0.1}\text{O}_3$ ) (see Fig. 3a). However, in the case of the pure Ti-6Al-4V coating deposited under the high-temperature spray conditions, there were no anatase peaks, but rutile peaks were present. Anatase peaks were present in the pure Ti-6Al-4V coating deposited under the low-temperature spray condition. High flame temperatures will promote the transformation of the meta-stable anatase phase of  $\text{TiO}_2$  to the stable rutile phase, with complete transformation at temperatures greater than approximately 700–1150 °C (Ref 18, 19).

The adiabatic flame temperatures are much greater than the recrystallization point of the bioactive glass for both sets of spray conditions. The absence of crystalline  $\text{Na}_2\text{Ca}_2\text{Si}_3\text{O}_3$  peaks under the low-temperature spray condition, and the recrystallization of the bioactive glass under the high-temperature spray condition can be explained by two possible mechanisms. The first mechanism is due to possible in-flight cooling of the particles between the torch and the substrate during deposition under the low-temperature spray conditions. During deposition with the low-temperature spray conditions, the torch is farther from the sample, compared to the high-temperature spray conditions. The increased distance allows additional convective cooling of the flame jet and the particles within the jet. The increased distance also allows entrainment of cold air into the flame jet. The larger temperature difference between the hot particles and cold air entrained into the flame results in higher cooling rates. This is supported by the presence of amorphous bioactive glass in the coating samples produced under the low-temperature spray

conditions, since higher cooling rates are necessary to prevent recrystallization and produce amorphous phases. The second mechanism may be due to the substrate temperature. During deposition under the high-temperature spray conditions, the torch is closer to the substrate, compared to the low-temperature spray conditions. The decreased distance results in additional heating of the substrate that was covered by the initial layers of the coating. The higher temperatures produced smaller temperature gradients between the substrate and the hot deposited particles. These smaller temperature gradients led to lower cooling rates, which produced recrystallized bioactive glass in the final coating. This mechanism is also supported by the presence of amorphous bioactive ceramic in the samples produced under the low-temperature spray conditions. Identification of the mechanism that plays a dominant role requires further study, but it is indisputable that the cooling rate of the bioactive ceramic particles is higher in the low-temperature deposition condition—otherwise the particles would not be amorphous after having been heated well above the recrystallization temperature.

### 3.2.2 Control and Bioactive Glass-Alloy Composite.

Coatings of ball-milled bioactive glass blended with Ti-6Al-4V and the control coatings of Ti-6Al-4V were examined with both optical and SEM. As sprayed, both compositions exhibited a porous and rough structure (see Fig. 4). The alloy-bioactive glass composite coating had a cross-sectional thickness ranging from 298 to 646  $\mu\text{m}$  with an average thickness of  $470 \pm 56 \mu\text{m}$  ( $n=12$ ). The control sample coatings (coatings of Ti-6Al-4V only) had a cross-sectional thickness ranging from 275 to 440  $\mu\text{m}$  with an average thickness of  $358 \pm 62 \mu\text{m}$  ( $n=7$ ). Figure 4 shows, for both compositions, a topographical SEM micrograph, in SE mode, and an optical cross-sectional micrograph, taken in BF mode.

In this study, it was assumed that the area fraction of porosity in the cross section is equivalent to the volume fraction of porosity in the entire coating. The area of the coating in the micrograph was measured as a percentage of the total micrograph area. The area of the porosity and bioactive glass as a percentage of the total micrograph area was divided by the area of the coating as a percentage of the total micrograph area. The calculation yielded the porosity and bioactive glass content as an area percentage of the coating only. The alloy-bioactive glass composite coating had a porosity of  $33 \pm 8 \text{ vol.}\%$  ( $n=7$ ) and a bioactive glass content of  $9 \pm 2 \text{ wt.}\%$  ( $n=7$ ). The Ti-6Al-4V coating had a porosity percent of  $26 \pm 6 \text{ vol.}\%$  ( $n=12$ ). The bioactive glass content of the coating, as determined by this analysis, is lower than the theoretical bioactive glass content of 15 wt.%, and the discrepancy could be due to removal of bioactive glass particles during polishing or non-homogeneity of the original powder blend.

The porosity and bioactive glass area distribution are plotted in Fig. 5. Analyses of areas (in  $\mu\text{m}^2$ ) were chosen due to the irregular shapes of the pores. A previous study by Klenke et al. (Ref 20) determined that significant osseointegration is not expected for pore sizes below 15,000  $\mu\text{m}^2$  (approximate effective diameter of 140  $\mu\text{m}$  for circular pores). Therefore, based on Fig. 5, significant cell

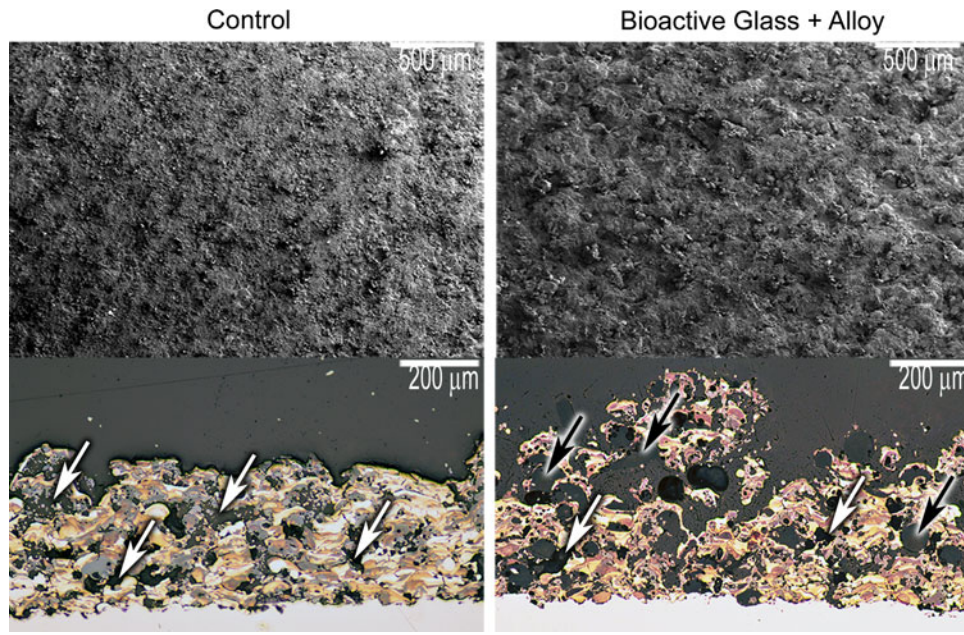


**Fig. 4** SEM topographical SE micrographs (top) and optical cross-sectional micrographs (bottom): left: Ti-6Al-4V control and right: bioactive glass-alloy blend. Black arrows indicate bioactive glass, white arrows indicate pores

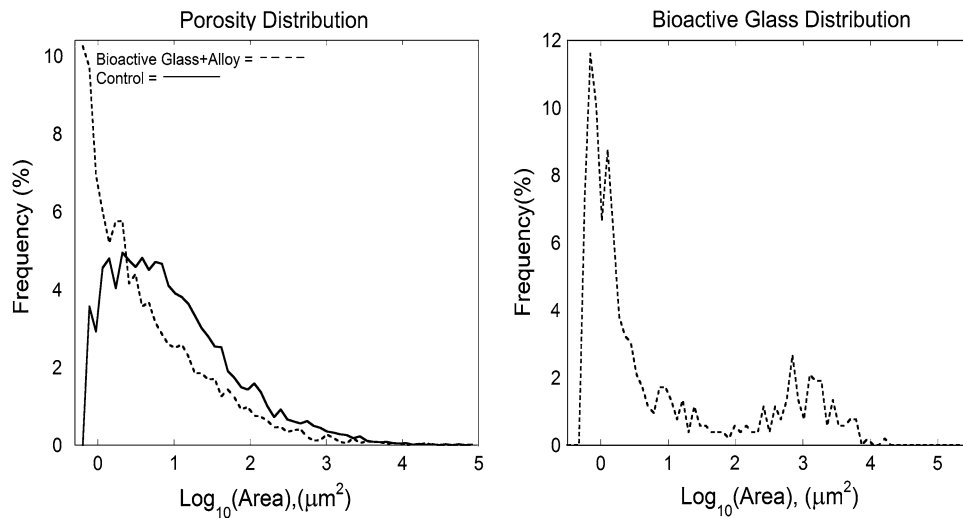


**Fig. 5** Left: pore distribution and right: bioactive glass distribution. Solid: Ti-6Al-4V control and dashed: bioactive glass-alloy blend

growth into pores would not be expected for either coating because the majority of the pores are clearly on the order of  $100 \mu\text{m}^2$  or less (effective diameter of  $11 \mu\text{m}$  for circular pores).

The bioactive glass area distribution was bimodal (see Fig. 5). The majority of the bioactive glass particles in the coatings had an area between  $1$  and  $100 \mu\text{m}^2$ ; a smaller portion, roughly 10% (see Fig. 5), had an area between  $100$  and  $10,000 \mu\text{m}^2$ . The second mode is closer to that which is expected with the given bioactive glass powder feed distribution. The first peak of the pore size distribution may indicate the fracture of bioactive glass particles

during deposition. The bioactive glass will dissolve in vivo (Ref 1) resulting in the creation of pores, however, the pore sizes formed through the dissolution of bioactive glass particles in the present coatings would be, on average, still too small for osseointegration to occur. Some bioactive glass particles are encapsulated in titanium alloy, as shown in Fig. 4. Hence, the encapsulated bioactive glass particles may not be exposed to the fluid environment. However, it should be noted that the *smallest* pore radius and pore interconnect will be the limiting factor in whether or not osseointegration is possible for any given pore (Ref 21).



Further work beyond this preliminary study will be required to maximize the pore sizes in the coatings and to assess the degree of pore interconnectivity. The size of the bioactive glass was also reduced by milling. All subsequent samples were flame-sprayed with the low-temperature parameters and with milled bioactive glass.

### 3.3 In Vitro Bioactivity Assessment

The 15 wt.% alloy-bioactive glass composite coating deposited under the low-temperature spray conditions

were selected for SBF testing. The selection was made on the basis of the possibility of pore connectivity for coatings deposited under the low-temperature spray parameters and bioactive glass crystallization under the high-temperature spray parameters. The crystallization of bioactive glass is undesirable as the dissolution rate in the aqueous environment is different (Ref 17). A study by Hench found that the dissolution rate of amorphous bioactive glass enables the bio-activity (Ref 2). Therefore, an amorphous form of bioactive glass is desired. The presence of pore interconnects is desirable as it allows osseointegration (Ref 21).

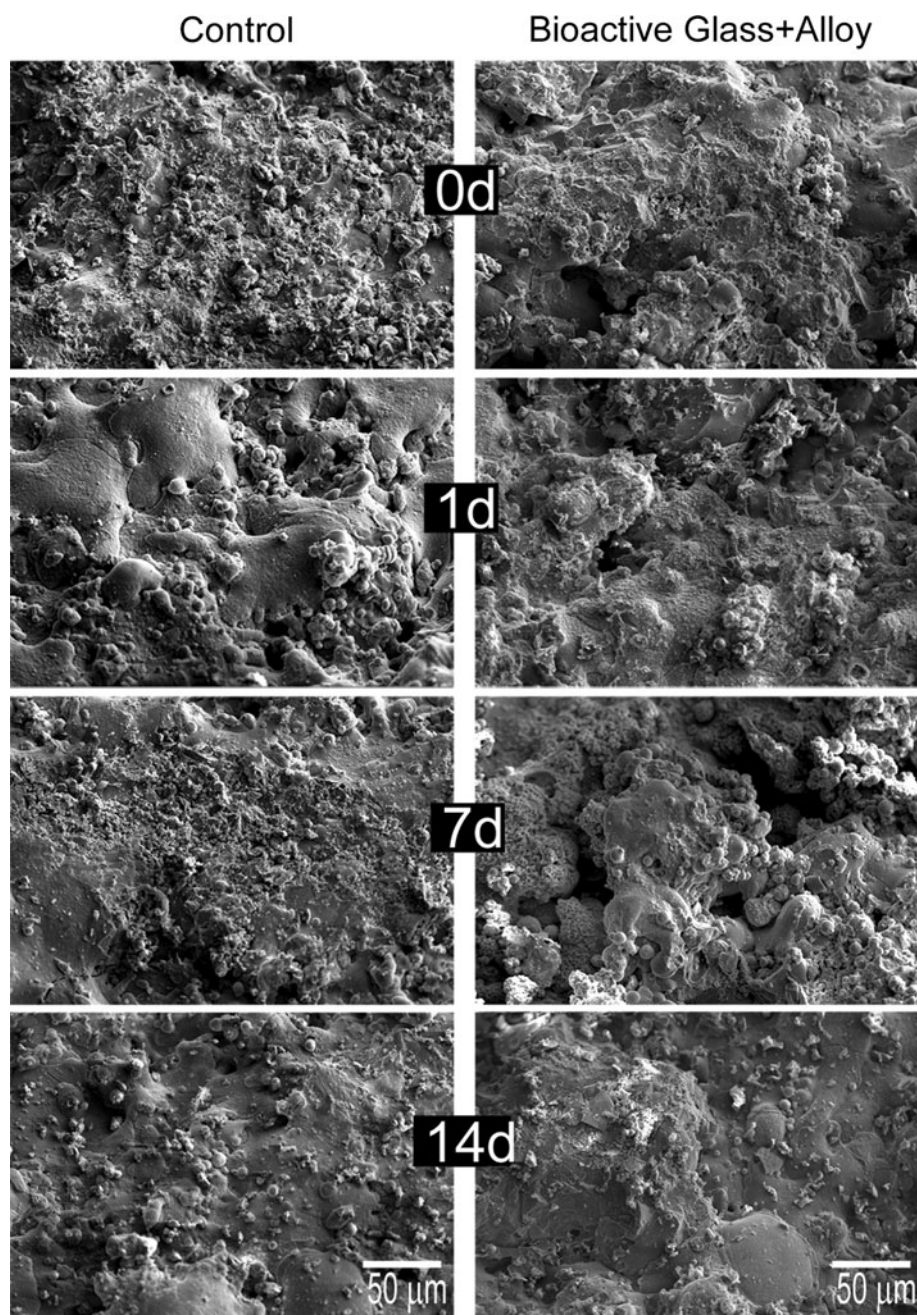


**Fig. 6** SEM micrographs of both the Ti-6Al-4V alloy control and bioactive glass-alloy blend exposed to SBF at 0, 1, 7, and 14 days: Left: control and right: bioactive glass-alloy blend

The control sample of Ti-6Al-4V coating was also used during SBF testing. The samples were treated in SBF for 0, 1, 7, and 14 days. One sample of each composition was immersed for each exposure time. The in vitro response of the bioactive glass-alloy composite and the alloy control coatings to SBF exposure was assessed using three techniques: SEM with EDX, FTIR, and XRD.

**3.3.1 Scanning Electron Microscopy with Energy Dispersive X-ray Spectroscopy.** The SEM micrographs in Fig. 6 show very little change for the alloy control over

the 14 days of SBF exposure. The micrographs show slow development of a surface layer of material on the alloy-bioactive glass composite coating, with the material change becoming evident after 7 days of exposure. A previous study by Boccaccini and Maquet (Ref 22) suggested that the layer is HA. When coupled with the EDX results shown in Fig. 7, it becomes clear that there is little change in the composition of the alloy control. However, there is a marked increase in calcium and phosphorous on the alloy-bioactive glass composite coating surface.

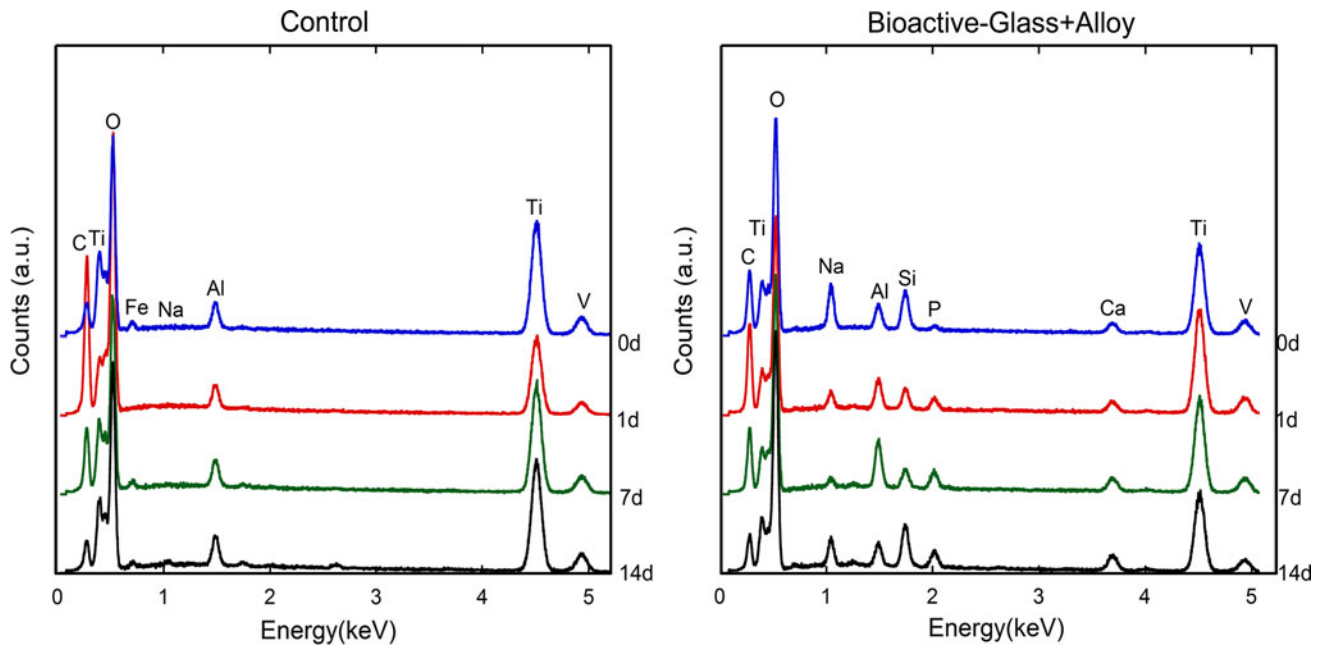


Fig. 7 EDX spectra: left: Ti-6Al-4V control and right: bioactive glass-alloy blend

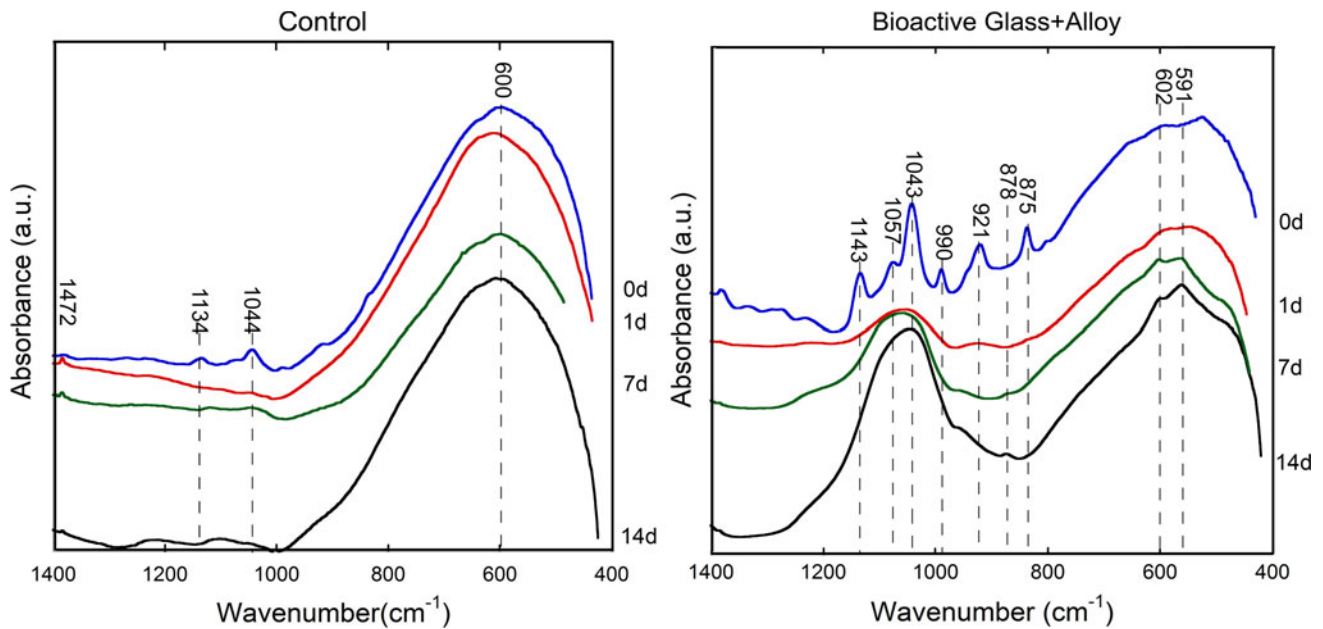
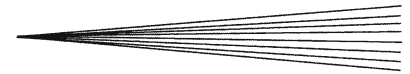


Fig. 8 FTIR spectra: left: Ti-6Al-4V control and right: bioactive glass-alloy blend



**Table 4 FTIR peaks assignments**

Bond type	Wave numbers, $\text{cm}^{-1}$	References
Si-O-Si	1057	24, 25
Ti-O	600	23
P-O (phosphate)	n3 1036-1095 n4 590 and 600	24-28
Carbonate	875	24-27
V-O ( $\text{V}_2\text{O}_3$ )	1044, 1134	29
Bioactive glass	1057, 921, 878	24, 25

The combination of both techniques suggests the formation of a surface layer with a chemical composition and structure similar to that of HA, however, SEM/EDX coupled with FTIR is the most effective and reliable method to identify HA in such systems.

**3.3.2 Fourier Transform Infrared Spectroscopy.** The FTIR spectra support the identity of the compounds formed on the surfaces of the bioactive glass-alloy composite coatings from in vitro testing as HA. The FTIR results are shown in Fig. 8 and the peak assignments are

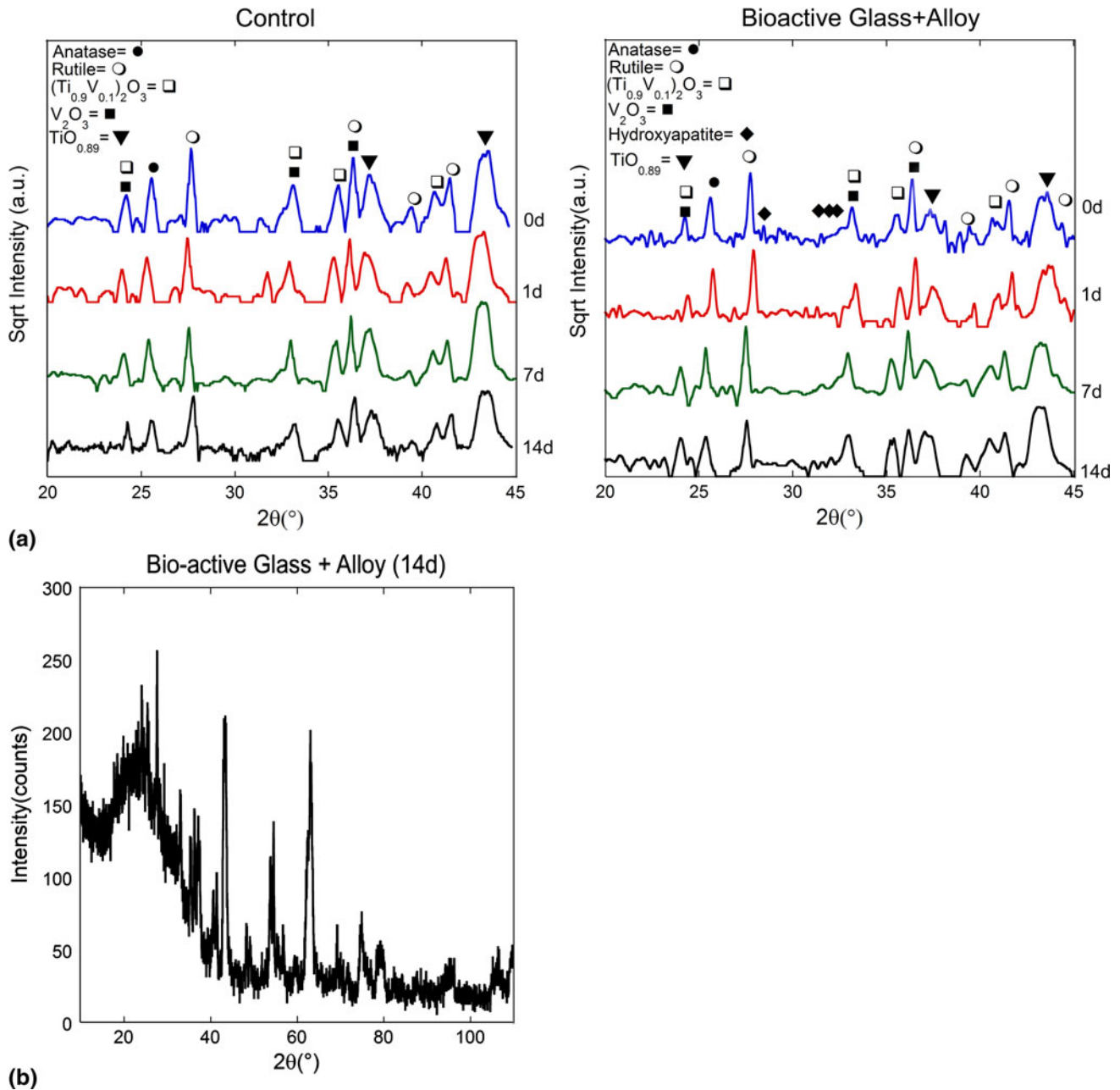


**Fig. 9** (a) XRD patterns: left: Ti-6Al-4V control, right: bioactive glass-alloy blend and (b) representative raw XRD pattern



presented in Table 4. In the Ti-6Al-4V control coating, there is no change in the peak profile as exposure time increased. The major broad band at approximately  $600\text{ cm}^{-1}$  is attributed to the presence of  $\text{TiO}_2$  (Ref 23). The series of bands between  $1250$  and  $1000\text{ cm}^{-1}$  is due to the presence of  $\text{V}_2\text{O}_3$ . In the bioactive glass-alloy composite coating, the bands corresponding to  $(\text{PO}_3)^{-4}$  ( $n=3$   $1050\text{ cm}^{-1}$ ,  $n=4$   $600\text{ cm}^{-1}$ , and  $n=4$   $560\text{ cm}^{-1}$ ) are observed after 7 days. Peaks were also observed for bioactive glass (Ref 24, 25) in the bioactive glass-alloy composite coatings. The peaks were assigned according to the procedures outlined by other investigators (Ref 23-29). The peak splitting of the  $600\text{-}550\text{ cm}^{-1}$  band is indicative of HA, as well as the carbonate peak at  $875\text{ cm}^{-1}$  (Ref 23-29). The FTIR spectra indicate the surface composition of the samples. The sample surfaces, before treatment, are predominately composed of  $\text{TiO}_2$ , bioactive glass, and  $\text{V}_2\text{O}_3$ . After treatment, there is very little change in the control coating surface composition. These results suggest that the bioactive glass-alloy composite coating initiates the formation of HA.

**3.3.3 X-ray Diffraction.** XRD patterns are shown in Fig. 9(a), where the background has been stripped and filtered to allow peak identification. A representative unstripped and unfiltered pattern has been included in Fig. 9(b). Peak assignments were determined according to the guidelines provided in the Jade 7 XRD database. The alloy control sample exhibited peaks for Ti, anatase, and rutile phases of  $\text{TiO}_2$  and  $\text{V}_2\text{O}_3$ . There were also peaks present that correspond to a  $\text{TiO}_{0.89}$  and a  $(\text{Ti}_{0.1}\text{V}_{0.9})_2\text{O}_3$ . There was no evidence of HA formation in the alloy control after any immersion time investigated. When coupled with the FTIR and SEM results, it became clear that no HA had formed on the Ti-6Al-4V alloy control after 14 days. The bioactive glass-alloy sample clearly shows evidence of crystalline HA formation after 14 days. The primary XRD peaks were observed at low intensities after 7 days of exposure to SBF. Additional formation of HA would require longer SBF exposure times.

## 4. Conclusions

This study demonstrates the effect of flame spray conditions on the phases and morphology of the flame-sprayed coatings produced by mixing 45S5 bioactive glass and Ti-6Al-4V powder. The low-temperature spray conditions were selected to prevent the bioactive glass from crystallizing and to increase the porosity of the coatings. The 15 wt.% bioactive glass-alloy blend was selected.

Work performed in this study demonstrates that flame-sprayed coatings produced by mixing 45S5 bioactive glass and Ti-6Al-4V powders results in in vitro surface mineralization of HA earlier than without the bioactive glass. The pore sizes in both coatings are likely too small for significant osseointegration to occur. However, the incorporation and eventual dissolution of bioactive glass may lead to the formation of larger pores to enhance mechanical interlocking of bone and the coating as bone grows in place of the bioactive glass.

It is the authors' opinion that this is a promising avenue of pursuit for further research in the area of biomedical implant coatings for bone fixation implants, although much future work remains. This study may open the way for coatings that are useful for load bearing applications such as permanent dental implants.

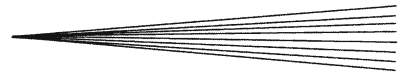
This study is preliminary and a more exhaustive investigation to increase pore size is required. This study does not consider the mechanical stability of the coatings and testing of the adhesion and fatigue behavior would be required. Other studies involving the surface mineralization rate and bio-mineral characteristics are also required. Studies regarding the attachment of cells on the surface must also be performed. Future work should focus on the mechanical stability and strength of the coating as well as improving the pore size and bioactive glass content of the coating.

## Acknowledgments

The authors acknowledge financial support from the Natural Sciences and Engineering Research Council of Canada (NSERC), the Government of Alberta Small Equipment Grants Program (SEGP), the Canada Foundation for Innovation (CFI), and the University of Alberta's Dean's Research Award Program. The authors gratefully acknowledge the contribution of bioactive glass powder from Mr. Ted Day at Mo-Sci Health Care Corporation, Michael Mahon for fabricating the original specimens used in this study, and the assistance of Mr. Wayne Moffat for FTIR, Ms. De-Ann Rollings for SEM, and Mr. Shiraz Merali for XRD tests.

## References

1. R.L. Reis, F.J. Monteiro, and G.W. Hastings, Stability of Hydroxylapatite Plasma-Sprayed Coated Ti-6Al-4V Under Cyclic Bending in Simulated Physiological Solutions, *J. Mater. Sci. Mater. Med.*, 1994, **5**, p 457-462
2. L.L. Hench, The Story of Bioglass®, *J. Mater. Sci. Mater. Med.*, 2006, **17**, p 967-978
3. L.L. Hench and H.A. Paschall, Direct Chemical Bond of Bioactive Glass-Ceramic Materials to Bone and Muscle, *J. Biomed. Mater. Res.*, 1973, **7**, p 25-42
4. T.K. Greenlee, C.A. Beckham, J.C. Malmorg, and A.R. Crebo, Glass Ceramic Bone Implant—Light Microscopic Study, *J. Biomed. Mater. Res.*, 1972, **6**, p 235-244
5. L. Jiang, X. Lu, Y. Leng, S. Qu, B. Feng, and J. Weng, Micro-patterned  $\text{TiO}_2$  Effects on Calcium Phosphate Mineralization, *Mater. Sci. Eng. C*, 2009, **29**, p 2355-2359
6. A. Rakngarm, Y. Miyashita, and Y. Mutoh, Formation of Hydroxyapatite Layer on Bioactive Ti and Ti-6Al-4V by Simple Chemical Technique, *J. Mater. Sci. Mater. Med.*, 2008, **19**, p 1953-1961
7. D.C. Greenspan and L.L. Hench, Chemical and Mechanical-Behavior of Bioglass-Coated Alumina, *J. Biomed. Mater. Res.*, 1976, **10**, p 503-509
8. T. Kokubo and H. Takadama, How Useful is SBF in Predicting In Vivo Bone Bioactivity?, *Biomaterials*, 2006, **27**, p 2907-2915
9. K. Ou, Y. Shih, C. Huang, C. Chen, and C. Liu, Preparation of Bioactive Amorphous-Like Titanium Oxide Layer on Titanium by Plasma Oxidation Treatment, *Appl. Surf. Sci.*, 2008, **255**, p 2046-2051



10. E. Verne, M. Ferraris, A. Ventrella, L. Paracchini, A. Krajewski, and A. Ravaglioli, Sintering and Plasma Spray Deposition of Bioactive Glass-Matrix Composites for Medical Applications, *J. Eur. Ceram. Soc.*, 1998, **18**, p 363-372
11. K.A. Gross, C.C. Berndt, and H. Herman, Amorphous Phase Formation in Plasma-Sprayed Hydroxyapatite Coatings, *J. Biomed. Mater. Res.*, 1998, **39**, p 407-414
12. B. Jeffery, M. Pepler, R.S. Lima, and A. McDonald, Bactericidal Effects of HVOF-Sprayed Nanostructured TiO<sub>2</sub> on *Pseudomonas aeruginosa*, *J. Therm. Spray Technol.*, 2010, **19**, p 344-349
13. H.H. Beherei, K.R. Mohamed, and G.T. El-Bassyouni, Fabrication and Characterization of Bioactive Glass (45S5)/Titania Biocomposites, *Ceram. Int.*, 2009, **35**, p 1991-1997
14. Y. Çengel and M. Boles, *Thermodynamics: An Engineering Approach*, 6th ed., McGraw-Hill, New York, 2008, p 936-950
15. O. Bretcanu, X. Chatzistavrou, K. Paraskevopoulos, R. Conrardt, I. Thompson, and A.R. Boccaccini, Sintering and Crystallisation of 45S5 Bioglass® Powder, *J. Eur. Ceram. Soc.*, 2009, **29**, p 3299-3306
16. D.C. Clupper and L.L. Hench, Crystallization Kinetics of Tape Cast Bioactive Glass 45S5, *J. Non-Cryst. Solids*, 2003, **318**, p 43-48
17. J.A. Nychka, S.L.R. Mazur, S. Kashyap, D. Li, and F. Yang, Dissolution of Bioactive Glasses: The Effects of Crystallinity Coupled With Stress, *JOM*, 2009, **61**, p 45-51
18. M. Stir, R. Nicula, and E. Burkel, Pressure-Temperature Phase Diagrams of Pure and Ag-Doped Nanocrystalline TiO<sub>2</sub> Photocatalysts, *J. Eur. Ceram. Soc.*, 2006, **26**, p 1547-1553
19. S. Bakardjieva, J. Subrt, V. Stengl, M. Dianež, and M. Sayagues, Photoactivity of Anatase-Rutile TiO<sub>2</sub> Nanocrystalline Mixtures Obtained by Heat Treatment of Homogeneously Precipitated Anatase, *Appl. Catal. B Environ.*, 2005, **58**, p 193-202
20. F.M. Klenke, Y. Liu, H. Yuan, E.B. Hunziker, K.A. Siebenrock, and W. Hofstetter, Impact of Pore Size on the Vascularization and Osseointegration of Ceramic Bone Substitutes In Vivo, *J. Biomed. Mater. Res. A*, 2008, **85A**, p 777-786
21. S.J.X. Lu, B. Flautre, K. Anselme et al., Role of Interconnections in Porous Bioceramics on Bone Recolonization In Vitro and In Vivo, *J. Mater. Sci. Mater. Med.*, 1999, **10**, p 111-120
22. A.R. Boccaccini and V. Maquet, Bioresorbable and Bioactive Polymer/Bioglass (R) Composites with Tailored Pore Structure for Tissue Engineering Applications, *Compos. Sci. Technol.*, 2003, **63**, p 2417-2429
23. P. Manivasakan, V. Rajendran, P.R. Rauta, B.B. Sahu, P. Sahu, B.K. Panda, S. Valiyaveettil, and S. Jegadesan, Effect of TiO<sub>2</sub> Nanoparticles on Properties of Silica Refractory, *J. Am. Ceram. Soc.*, 2010, **93**, p 2236-2243
24. M.H. Fathi, A. Hanifi, and V. Mortazavi, Preparation and Bioactivity Evaluation of Bone-Like Hydroxyapatite Nanopowder, *J. Mater. Process. Technol.*, 2008, **202**, p 536-542
25. I. Rehman, M. Karsh, L.L. Hench, and W. Bonfield, Analysis of Apatite Layers on Glass-Ceramic Particulate Using FTIR and FT-Raman Spectroscopy, *J. Biomed. Mater. Res.*, 2000, **50**, p 97-100
26. A. Slosarczyk, Z. Paszkiewicz, and C. Paluszkiwicz, FTIR and XRD Evaluation of Carbonated Hydroxyapatite Powders Synthesized by Wet Methods, *J. Mol. Struct.*, 2005, **744**, p 657-661
27. W.J. Wu and G.H. Nancollas, Kinetics of Nucleation and Crystal Growth of Hydroxyapatite and Fluorapatite on Titanium Oxide Surfaces, *Colloids Surf. B*, 1997, **10**, p 87-94
28. E. Kontonasaki, T. Zorba, L. Papadopoulou, E. Pavlidou, X. Chatzistavrou, K. Paraskevopoulos, and P. Koidis, Hydroxy Carbonate Apatite Formation on Particulate Bioglass In Vitro as a Function of Time, *Cryst. Res. Technol.*, 2002, **37**, p 1165-1171
29. L.D. Frederickson and D.M. Hausen, Infrared Spectra-Structure Correlation Study of Vanadium-Oxygen Compounds, *Anal. Chem.*, 1963, **35**, p 818